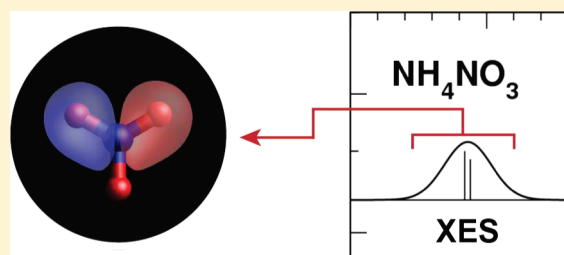


## X-ray Emission Spectroscopy of Nitrogen-Rich Compounds

Fernando D. Vila,<sup>\*</sup> Terrence Jach,<sup>†</sup> W. T. Elam,<sup>‡</sup> John J. Rehr,<sup>\*</sup> and J. D. Denlinger<sup>§</sup><sup>\*</sup>Department of Physics, University of Washington, Seattle, Washington 98195, United States<sup>†</sup>Material Measurement Laboratory, National Institute of Standards and Technology, Gaithersburg, Maryland 20899, United States<sup>‡</sup>Applied Physics Laboratory, University of Washington, Seattle, Washington 98195, United States<sup>§</sup>Advanced Light Source, Lawrence Berkeley National Laboratory, Berkeley, California 94720, United States

## Supporting Information

**ABSTRACT:** Nonresonant X-ray emission spectroscopy was used to compare the nitrogen-rich compounds ammonium nitrate, trinitrotoluene, and cyclotrimethylene–trinitramine. They are representative of crystalline and molecular structures of special importance in industrial and military applications. The spectral signature of each substance was analyzed and correlated with features in the electronic structure of the systems. This analysis was accomplished by means of theoretical simulations of the emission spectra and a detailed examination of the molecular orbitals and densities of states. We find that the two theoretical methods used (frozen-orbital density functional theory and real-space Green's function simulations) account semiquantitatively for the observed spectra and are able to predict features arising from distinct chemical complexes. A comparison of the calculations and the data provides insight into the electronic contributions of specific molecular orbitals, as well as the features due to bandlike behavior. With some additional refinements, these methods could be used as an alternative to reference compounds.



## I. INTRODUCTION

The intensity, stability, and energy range of third-generation synchrotron radiation sources has contributed enormously to the progress of X-ray spectroscopy.<sup>1,2</sup> The tunable, continuous flux of X-ray photons produced by these sources makes possible the selective excitation of a wide variety of chemical compounds and the observation of new phenomena. When combined with high-resolution monochromators and spectrometers, different aspects of the electronic structure of a system can be addressed with these methods: X-ray absorption (XAS) and resonant inelastic X-ray scattering (RIXS) to probe the unoccupied density of states associated with a selected absorber, X-ray emission spectroscopy (XES),<sup>3,4</sup> and X-ray fluorescence (XRF) to probe the occupied valence states.

High-resolution emission spectroscopy is particularly valuable with initial states involving the valence band because they directly reveal the chemical bonding environment associated with the selected absorber, facilitating the connection with ground-state theoretical electronic structure methods.<sup>5</sup> The valence band density of states can span 20 eV or more of an X-ray emission spectrum, so it is not accessible to optical or infrared spectroscopy.

Features observed in XES and XRF have the added advantage that they can be measured in spectra produced when electron microscopes or X-ray tubes create the required core-holes.<sup>6</sup> Thus, details observed under conditions of selective excitation and high resolution can frequently supply insight in widespread applications, even those resulting in spectra of lower resolution

and intensity.<sup>7</sup> Examples of these are the locations of Fermi edges, densities of states (DOS), chemical shifts, and spatial distributions of valence charge.

As with most other spectroscopic techniques, XES has undergone a historical progression in which the interpretation of spectra has become more and more sophisticated, evolving from the study of simple qualitative similarities, to the use of reference systems, to the introduction of highly successful computational methods for the simulation of the spectra. Furthermore, experimental technology has advanced as well. In addition to conventional grating or crystal spectrometers, new high-resolution microcalorimeter X-ray detectors make it possible to collect X-ray spectra from multiple elements in a compound.<sup>8</sup>

The goal of this article is 2-fold: First, we propose to study the role that these theoretical methods can play in interpreting complex XES spectra of nitrogen compounds. We pay special attention to contrasting theoretical approaches that maximize the overall understanding of a system. We are interested here in the relative merit of localized molecular orbital calculations versus real-space calculations at a manageable level. Second, we will explore the possibility of theoretically determining the spectroscopic fingerprints of certain chemical complexes. Our aim is to

Received: September 7, 2010

Revised: January 31, 2011

Published: March 31, 2011

facilitate the identification of unknown substances and to reduce the reliance on reference compounds.

For this purpose, we will focus on three examples that represent different classes of nitrogen-rich compounds that have not been studied by XES: ammonium nitrate,  $\text{NH}_4\text{NO}_3$ , an ionic compound of nitrate and ammonium groups, each with inequivalent crystalline nitrogen sites; trinitrotoluene,  $\text{C}_7\text{H}_5\text{N}_3\text{O}_6$ , (TNT), a molecular compound with nitro groups in inequivalent sites; and cyclotrimethylene-trinitramine,  $\text{C}_3\text{H}_6\text{N}_6\text{O}_6$ , (RDX), a molecular compound with nitro and azine nitrogens. Nitrogen-rich molecules are central to a wide variety of scientific, industrial, and military applications. They are widespread in biological systems, where they form the basis of proteins (aminoacids) and nucleic acids (nucleobases).<sup>9–11</sup> In these systems, the nitrogen atoms appear mostly in amine groups and as part of aromatic rings. Nitrogen is also present in amino, azine, and nitro groups in highly energetic materials like propellants and explosives. The materials of interest in the present study belong to this class of compounds. XES is well suited for the study of chemical reactivity, speciation, and predisposition to radiation damage, all aspects of electronic structure of special interest in the case of explosive materials.

When assisted by theoretical interpretation methods, XES is also appropriate for determining correlations in subtle changes around the absorbing atom. From a more practical perspective, XES might eventually replace less sophisticated tools for the identification of substances of forensic interest in facility protection, cargo inspection, military ordnance, and counter-terrorism.<sup>12</sup> Fluorescence techniques possess a distinct advantage since they are bulk sensitive and require minimal sample preparation. The principal challenge resides in that similar chemical moieties are shared by many explosives and common organic compounds, thus making them difficult to identify over a background of everyday substances. Therefore, a clear understanding of the expected spectral fingerprints (and their variations) would be very useful.

## II. METHODS

**A. Experimental Methods.** X-ray absorption and emission spectra were obtained from all samples on the spectroscopy undulator beamline 8.0.1 at the Advanced Light Source. The beamline is comprised of a focusing spherical grating monochromator and a spherical grating spectrometer on a Rowland circle with a microchannel plate detector.<sup>13</sup>

We calibrated the monochromator using the N K-absorption spectrum of  $\text{N}_2$  gas embedded in ZnO. The multiple vibrational bands were fitted using a value for the peak corresponding to the initial  $1s-1\pi_g^*$  band transition of 400.70 eV.<sup>14</sup> The standard uncertainty of monochromator energy from the fit to the bands was 0.08 eV. Elastic scattering from each of the samples at several energies was used to calibrate the emission spectrometer. A linear correction was applied, yielding a standard energy uncertainty of the emission spectra of 0.09 eV. One emission spectrum, that of  $\text{NH}_4\text{NO}_3$ , dates from a previous run in which the monochromator energy was calibrated, but the emission spectrometer was not. While its absorption spectrum has the same accuracy as the other spectra, in the interests of caution we have assigned an overall uncertainty of 2 eV to the energy scale of that emission spectrum.

Samples of  $\text{NH}_4\text{NO}_3$  were prepared by pressing the fine powder (99.89% purity) into In foil. Samples of TNT (99.9% purity) and RDX (99.2% purity) were prepared by evaporating solutions of the compounds from a commercial standards supplier at a concentration of 20 mg/mL of acetone onto In foil.

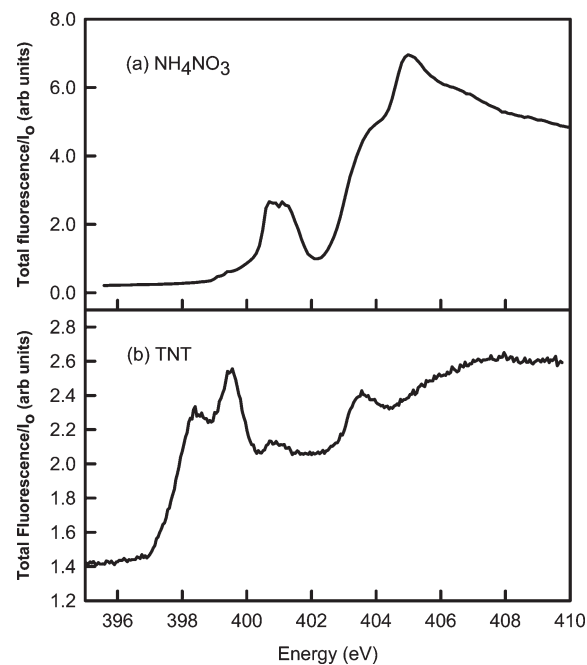


**Figure 1.** (a) X-ray absorption spectrum of  $\text{NH}_4\text{NO}_3$ , (b) X-ray absorption spectrum of TNT.

The absorption spectra were obtained by measuring the total X-ray fluorescence yield from a sample with a channeltron biased to reject photoelectrons. The absorption spectra were obtained in steps of 0.1 eV with 0.5 s intervals. The absorption spectra from  $\text{NH}_4\text{NO}_3$  and TNT are shown in parts a and b of Figure 1. The absorption spectra typically show an excitonic feature near the nitrogen K edge and a continuum spectrum above that.

The absorption spectra of these two compounds show very different structure. In particular, the N 1s K edge is significantly lower ( $\sim 2$  eV) for TNT. The observations of transitions into low-lying LUMO states has been documented in other energetic nitrogen compounds as well.<sup>15</sup> Similar absorption spectra obtained from the compounds  $\text{NaNO}_2$  and  $\text{NaNO}_3$  showed *double* sharp exciton-like peaks. We concluded that this was due to real-time oxidation of  $\text{NaNO}_2$ <sup>16</sup> and reduction of the  $\text{NaNO}_3$ <sup>17</sup> under the action of the excitation beam. Spectra taken elsewhere with continuous deposition of the compounds from an effusion cell minimized the extra peaks.<sup>16,18</sup> The spectra of  $\text{NaNO}_2$  and  $\text{NaNO}_3$  were thus not included in this study. The spectra of  $\text{NH}_4\text{NO}_3$ , TNT, and RDX did not show the additional features. This is because any reduction products are volatile and do not remain on the samples. We are confident that the emission spectra of these compounds reflect only the presence of the original compounds.

The emission spectra in this article were obtained by excitation with the incident beam monochromator tuned to the vicinity of 425 eV. The energy was chosen to be sufficiently high such that 1) correlation effects between absorption and emission were minimized, 2) effects of angular anisotropy of the atomic potential were minimized, and 3) the oscillator strength of emission was not a sensitive function of the excitation energy. XES obtained in this way are not dissimilar from electron-excited XES.

The samples were located on one point of a Rowland circle that also included a spherical grating with a pitch of 1500 lines/mm and a position-sensitive microchannel plate to collect the photons. The acceptance of the microchannel plate was such

that the energy range covered (depending on the slit settings) was 20–40 eV over 512 channels. The entire emission spectrum from the valence band was thus recorded all at once. The total recording time for the  $\text{NH}_4\text{NO}_3$  was 1800 s. The total recording times in the case of TNT and RDX were 1200 s each.

**B. Theoretical Methods.** The nonresonant emission intensity of a photon of energy  $\omega$  and polarization  $\hat{\epsilon}$  is proportional to the radiative decay rate:

$$w = \frac{\alpha^3 \omega^3}{2\pi} \sum_i | \langle c | \hat{\epsilon} \cdot \vec{r} | i \rangle |^2 \times \delta(\omega + E_c - E_i) \quad (1)$$

where we have assumed that the single-particle and dipole approximations are valid,  $c$  and  $i$  represent final (core) and initial (valence) single-particle states,  $\alpha$  is the fine structure constant, and atomic units are used. The calculation of the decay rate can be carried out in different ways. For instance, the transition dipole moments  $\langle c | \vec{r} | i \rangle$  can be calculated directly within the frozen-orbital approximation as implemented in the StoBe-deMon<sup>19</sup> density functional theory (DFT) code. In this case, the single-particle states are Kohn–Sham molecular orbitals. The excited states are formed from the ground state orbitals and are represented by a single Slater determinant. Alternatively, the sum over valence states in eq 1 can be carried out efficiently by introducing the Green's function operator  $G(\omega)$ :

$$w = -\frac{\alpha^3 \omega^3}{2\pi^2} \text{Im} \langle c | \hat{\epsilon} \cdot \vec{r} : G(\omega) : \vec{r} \cdot \hat{\epsilon} | c \rangle \quad (2)$$

Eq 2 is analogous to Fermi's golden rule for X-ray absorption spectroscopy as implemented in FEFf.<sup>20,21</sup> FEFf is based on a real-space representation of the quasi-particle Green's function (RSGF) and is applicable to both periodic and aperiodic systems. Atomic structures represented by muffin-tin potentials are treated by full multiple scattering, leading to bandlike densities of states.

These approaches differ in three important ways: First, the RSGF approach in FEFf involves a spherically averaged muffin-tin approximation to the full potential. This approximation can potentially affect orbital energies near the Fermi level in molecular systems with highly directional covalent bonds. However, the frozen-orbital method implemented in StoBe-deMon uses a full potential. Thus, comparison of the densities of states and spectra obtained with this method help gauge the accuracy of the results obtained with the spherical muffin-tin method.

Second, the method implemented in StoBe-deMon is limited by the size and type of systems to which it can be applied. For example, extended systems such as solids can be computed only as long as the cluster models used in the DFT simulations provide a good representation of the full system. However, the FEFf multiple scattering approach has been widely and successfully applied to extended systems. Moreover, the use of the RSGF in FEFf avoids the explicit calculation of the quasi-particle wave functions, making this approach very efficient. The solid systems studied in the present work are ideally suited given that the molecular nature of their electronic structure make them easy to represent using clusters.

Finally, both approaches differ in the kind of chemical information that can be extracted about each of the transitions involved. This aspect will be discussed in more detail when the results for  $\text{NH}_4\text{NO}_3$  are presented below. Briefly, in the frozen-orbital approach, the molecular orbitals involved in each transition can be readily identified and assigned to specific molecular moieties. This provides a wealth of information and allows us to

make predictions regarding transitions in systems with similar chemical structure. The RSGF method, however, directly computes the measured quantity, the full spectrum, without an intermediate calculation of the individual transitions. Thus, structural information has to be obtained indirectly by projecting the density of states onto individual atomic sites.

In summary, these methods provide independent validation of the theoretical results and offer complementary views that, when combined, result in a more complete understanding of the systems of interest.

**C. Computational Details.** All simulations used clusters derived from the experimentally determined crystallographic structures.<sup>22–24</sup> The FEFf simulations used full multiple scattering (FMS) clusters of radius 9 Å, centered on each absorbing site. The self-consistent scattering potentials were calculated using smaller clusters of radius 5 Å, with different potentials for each of the symmetry-unique centers in the crystal. These cluster sizes ensured the convergence of the results. For the molecular ionic system ( $\text{NH}_4\text{NO}_3$ ), the StoBe-deMon simulations used only those atoms inside a unit cell (i.e., two pairs of molecular ions). Exploratory calculations with larger clusters revealed that a single unit cell embedded in a 40 Å × 30 Å × 30 Å volume filled with background point charges was sufficient to obtain convergence of the calculation. In the case of TNT and RDX, which are neutral molecular systems, we find that single-molecule calculations give converged results, even though in TNT there are two symmetry-inequivalent molecules. Nevertheless, the results presented here correspond to averages over all symmetry-unique absorbing sites in a unit cell. The StoBe-deMon simulations used the IGLO-III<sup>25</sup> basis set for the absorbing atoms, whereas the TZV<sup>26</sup> basis set was used for the rest. The Coulomb and exchange correlation potentials were fitted and expanded over auxiliary basis sets with ( $N_C(s)$ ,  $N_C(\text{spd})$ ;  $N_{XC}(s)$ ,  $N_{XC}(\text{spd})$ )  $s$  and  $\text{spd}$ -type functions. Auxiliary sets of (5,2;5,2) quality were used for the C, N, and O atoms, and of (3,1;3,1) quality for the H atoms. The gradient-corrected BP86 functional was used<sup>27,28</sup> for all StoBe-deMon calculations, and the Hedin–Lundqvist self-energy<sup>29</sup> was used for all FEFf simulations. Finally, the spectra were uniformly broadened to match experimentally observed broadening of the principal features.

Auxiliary calculations were used to determine the background charges included in the StoBe-deMon simulations, and to position accurately the Fermi energy obtained in the FEFf simulations with respect to features in the density of states (DOS). These calculations were performed with the plane-wave package VASP.<sup>30</sup> Briefly, using the PBE<sup>31</sup> exchange-correlation functional, the DOS was calculated for a cell generated by repeating the unit cell 3 × 3 × 3 times. The DOS from both FEFf and VASP were then aligned to determine an appropriate correction for the FEFf calculations. Figure 2 shows typical results for  $\text{NaNO}_2$ . For systems containing only NO and NC bonds, the required corrections were very consistent, amounting to ~2.5 eV, whereas for  $\text{NH}_4\text{NO}_3$ , the correction was 3.8 eV. Moreover, standard FEFf calculations use core orbital energies calculated for the isolated atom, thus neglecting the core chemical shifts. In the case of compounds with final states in the amino or azine, and nitro groups, this approximation results in spectra with incorrect relative splitting. To avoid this problem, we have improved FEFf's account of the core energies by calculating them for the embedded atom. This can be easily achieved by searching for the pole in the Green's function corresponding to the core state, and gives shifts of 4.3 eV for the amino and 4.5 eV for the azine

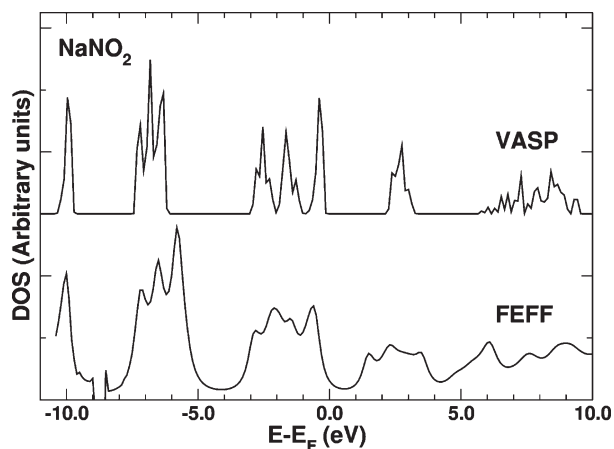


**Figure 2.** Comparison of the density of states of  $\text{NaNO}_2$  calculated with plane-wave (VASP) and RSMS (FEFF) methods. The energy scale has been shifted to place the origin at the Fermi energy in both simulations.

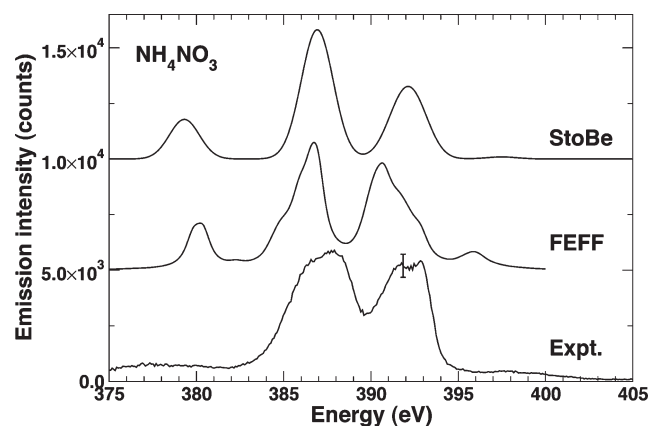


**Figure 3.** Experimental and theoretical  $\text{N-K}\alpha$  XES spectra of  $\text{NH}_4\text{NO}_3$ .

groups. These values are in excellent agreement with the shifts obtained from the core energy differences in the StoBe-deMon simulations. After these corrections are applied, no *ad hoc* shifts are required to match the FEFF results with the experimental spectra. Finally, in addition to providing improved Fermi energies, the electron density distributions from the VASP calculations were analyzed using Bader decomposition<sup>32</sup> and used to generate a set of background atomic charges for the ionic systems.

### III. RESULTS

**A.  $\text{NH}_4\text{NO}_3$ .** Ammonium nitrate is a particularly interesting example for several reasons: First, the experimental spectrum is well resolved, making the assignment of the distinct peaks relatively simple. Second, from a chemical point of view, the nitrogen atoms in  $\text{NH}_4\text{NO}_3$  are quite distinct and representative of two extremes, that is, highly oxidized ( $\text{NO}_3^-$ ) and highly reduced ( $\text{NH}_4^+$ ). Finally, the lack of covalent bonding between the two ions results in spectral signatures that are easily separated, thus simplifying the matching of features in the valence electronic structure to those in the emission spectra, as well as to features observed in closely related compounds. We will therefore pay particular attention to the analysis of its spectrum.

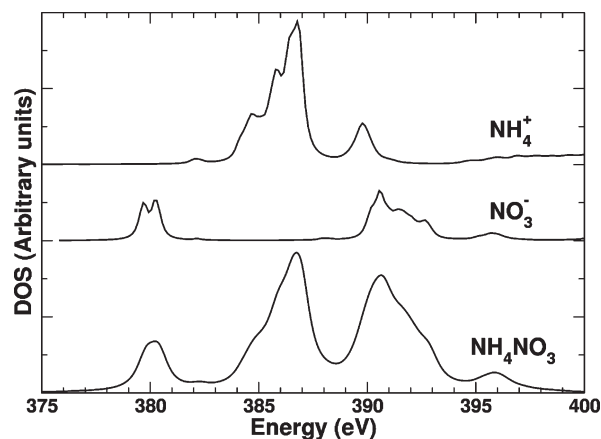


**Figure 4.** Comparison of the FEFF theoretical  $\text{N-K}\alpha$  XES spectra of  $\text{NH}_4\text{NO}_3$  to the  $p$ -component of density of states projected on the  $\text{NO}_3^-$  and  $\text{NH}_4^+$  N atoms.

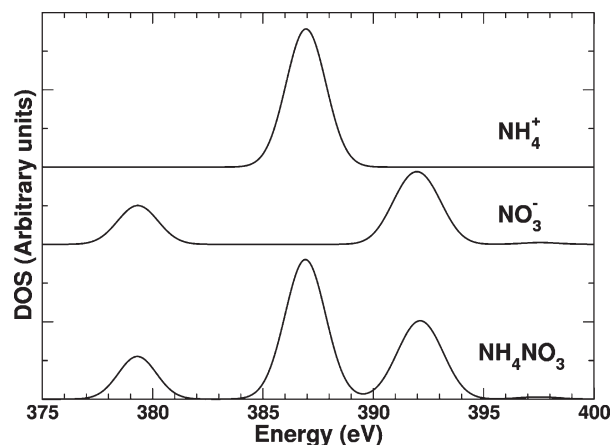


**Figure 5.** Decomposition of the StoBe-deMon theoretical  $\text{N-K}\alpha$  XES spectra of  $\text{NH}_4\text{NO}_3$  obtained by calculating each ion independently.

Figure 3 shows the experimental X-ray emission spectrum of  $\text{NH}_4\text{NO}_3$  as well as the average simulated spectra calculated using StoBe-deMon and FEFF. The experimental spectrum is dominated by two intense features around 387 and 392 eV that are well reproduced by both theoretical methods. A Gaussian fitting of these features reveals that they are composed of at least four dominant transitions, centered at 386.6 eV, 388.2 eV, 391.7, and 393.0 eV.

With the help of the theoretical simulations, the origin of each transition can be studied in several ways. Given the local nature of the XES probe, insight can be obtained by comparing the FEFF spectra to the site- and angular momentum-projected density of states. Figure 4 shows the full spectrum, along with the  $p$ -DOS projected on the  $\text{NO}_3^-$  and  $\text{NH}_4^+$  N atoms, shifted by the binding energy of the  $\text{N-K}\alpha$  state.

If the system can be separated into noncovalently bonded units, the spectrum of each individual component can be calculated and compared to that for the full system. Thus, for  $\text{NH}_4\text{NO}_3$  we can calculate the spectra of the  $\text{NO}_3^-$  and  $\text{NH}_4^+$  molecular ions. This approach is illustrated in the spectra plotted in Figure 5, where the StoBe-deMon spectrum is decomposed. Of the four peaks observed in the spectrum of  $\text{NH}_4\text{NO}_3$ , those at 379, 392, and 397 eV are the result of emission from the  $\text{NO}_3^-$

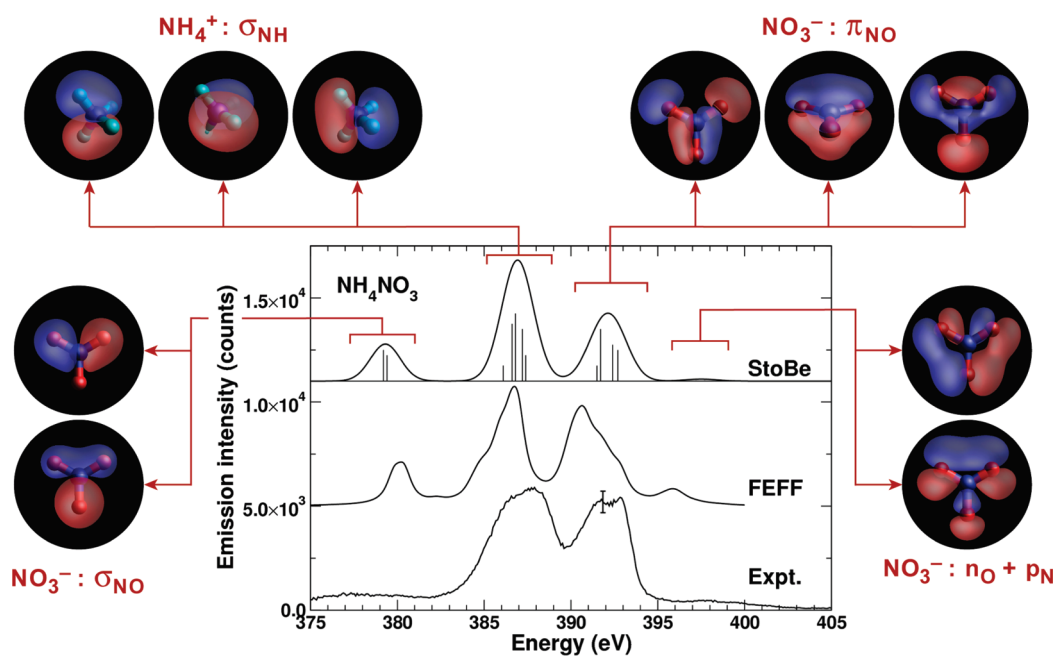


**Figure 6.** Composite spectra calculated by StoBe and FEFF compared to experimental results for  $\text{NH}_4\text{NO}_3$ . The contribution of orbitals in the StoBe calculation to features in the emission spectrum is indicated.

ion, whereas the one at 387 eV originates from the  $\text{NH}_4^+$  ion. The two methods are clearly consistent, confirming the assignment of the features.

The analysis of the local density of states and the separation of the spectrum into individual components represent simple ways in which features of a spectrum can be assigned. Nevertheless, they are limited in their applicability and in the amount of information they provide. Significantly more instructive is the analysis of the molecular orbitals involved in each transition.

Figure 6 shows such orbitals and their relation to features in the spectrum. Given the weak interaction between the molecular ions, the orbitals can be easily separated into those localized on the  $\text{NO}_3^-$ , and those on the  $\text{NH}_4^+$ . The intense peak at 391.7 eV corresponds to emission from the out-of-plane  $\pi_{\text{NO}}$  bond orbital, while the 392.5 eV transition originates from in-plane  $\pi_{\text{NO}}$ -like orbitals formed from the distorted diatomic  $\pi_{\text{NO}}$  orbitals. The out-of-plane component has a significantly larger  $p$ -like character on the N atom, resulting in emission intensities twice as large as those originating from the in-plane components. The features at 386.7 and 387.3 eV are associated with emissions from  $\sigma_{\text{NH}}$  orbitals. These features show very similar relative intensities due to the nearly identical  $p$ -like character on the N atom and quasi-symmetry of the orbitals. The broad peak at 379.3 eV corresponds to the more bound  $\sigma_{\text{NO}}$  orbitals, whereas the feature at 397.5 eV is associated with the weak coupling between the  $p_{\text{N}}$  atomic orbital and the nonbonding lone-pair orbitals on the O atoms.

The real space and molecular orbital results reveal good qualitative agreement between the theories, with equivalent features present in both approaches. The most noticeable differences are the slightly more structured spectrum given by the real-space approach and small differences in the transition energies. For instance, in the real-space calculations the transitions associated with the  $\sigma_{\text{NO}}$  bonds appear at slightly higher energy ( $\sim 0.9$  eV) and the splitting between the  $\pi_{\text{NO}}$  and  $\sigma_{\text{NH}}$  bonds is reduced (by about 1 eV). The high-energy features associated with nonbonding orbitals also show a shift of about

1.5 eV, but in the opposite direction. These differences likely arise from the use of the muffin-tin approximation in the FEFF calculations. This approximation tends to specially affect shallow, highly directional covalent bonds. Splitting differences of the same order of magnitude can be observed in the density of states shown in Figure 2 (cf. the  $-10$  to  $-5$  eV region).

Finally, the spectra of the individual components can be compared to those of related compounds. For instance, the transitions originating from the  $\text{NO}_3^-$  ion in  $\text{NH}_4\text{NO}_3$  are in very good agreement with those reported for  $\text{LiNO}_3$ ,<sup>33,34</sup> after a 2.1 eV overall redshift is applied. This shift likely arises from variations in the Fermi energy as well as chemical shifts between the  $\text{NO}_3^-$  N atom in  $\text{NH}_4\text{NO}_3$  and  $\text{LiNO}_3$ . For instance, in the case of  $\text{NaNO}_3$  we find a change of 1.4 eV in the Fermi energy, with an additional 0.3 eV due to chemical shifts. Preobrajenski et al.<sup>33</sup> observed the same fingerprint of one intense and two weak features. The weak features appear at 378.9 and 397.8 eV, compared to the 378.5 and 397.3 eV transitions observed here. The intense feature is well resolved, with peaks at 390.7 and 393.0 eV. Our calculations in  $\text{NaNO}_3$  show that the latter peak is analogous to the  $\text{NH}_4\text{NO}_3$  transition at 393.0 eV. The origin of the 390.7 eV peak is more uncertain. In principle, it could be assigned to the  $\text{NH}_4\text{NO}_3$  transition at 391.7 eV. A more plausible explanation, however, is to assume that this peak arises from the presence of  $\text{NO}_2^-$ , which is known to form from decomposition of the nitrate. Our results for  $\text{NaNO}_2$  and  $\text{NaNO}_3$  show that the  $\pi_{\text{NO}}$  transitions in  $\text{NO}_3^-$  are red-shifted by about 2 eV, bringing them close to the peak observed in  $\text{LiNO}_3$ . Finally, it should be noticed that the relative intensities of the relevant transitions (i.e., those calculated at 378.5, 393.0, and 397.3 eV) also show good agreement between theory and experiment.

**B. TNT.** Although sharing some similarities with the compound discussed above, TNT is significantly more complex. For instance, there are two symmetry unique molecules in the unit cell and each possesses three inequivalent emitters. Nevertheless, the local structure surrounding these six N atoms is similar, resulting

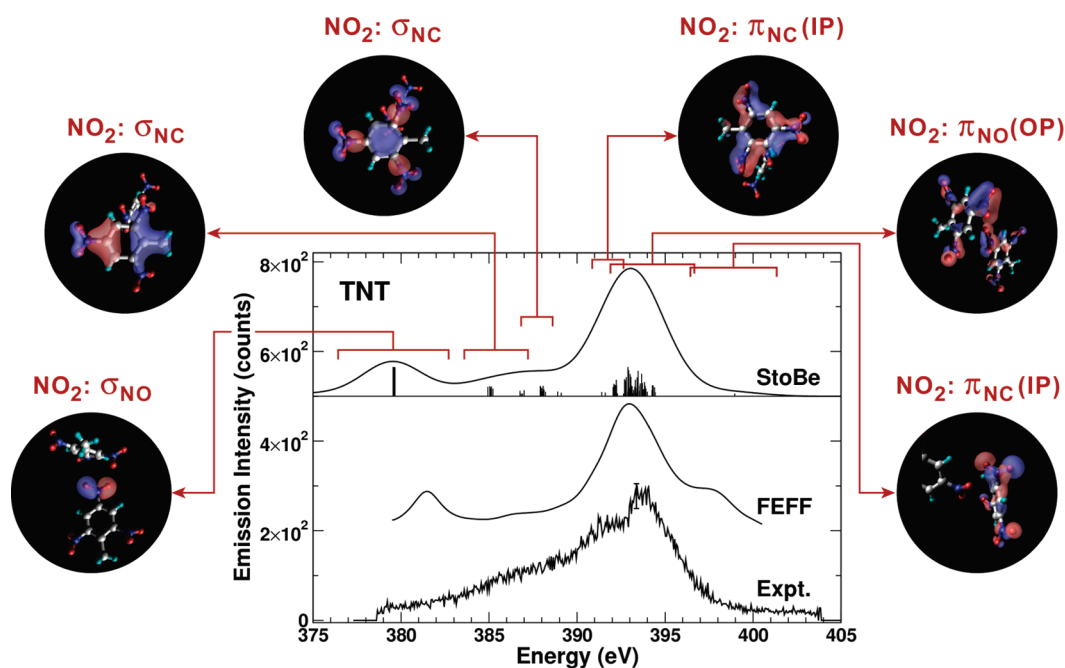


**Figure 7.** Composite spectra calculated by StoBe and FEFF compared to experimental results for TNT. The contribution of orbitals in the StoBe calculation to features in the emission spectrum is indicated.

in nearly equivalent spectra. Figure 7 shows the experimental and average simulated spectra. Location of the features of highest intensity can be provided by fitting with five Gaussians centered at 380.0, 389.6, 391.2, 393.7, and 394.2 eV. Because each N atom belongs to a  $\text{NO}_2$  group bound to an aromatic C atom, these spectra display characteristics that are intermediate to those found in the  $\text{NO}_2^-$  and  $\text{NO}_3^-$  anions. For example, the theoretical calculations show that the most intense features, at 393.7 and 394.2 eV in the experiment and in the 393.0 to 394.4 eV region for the theoretical calculations, are composed of emissions from the in-plane and out-of-plane  $\pi_{\text{NO}}$  and  $\pi_{\text{NC}}$  orbitals. The theoretical spectra also show the low energy feature (at 379.5 and 381.2 eV for StoBe-deMon and FEFF, respectively) associated with the  $\sigma_{\text{NO}}$  orbitals. As in the case of  $\text{NO}_2^-$  and  $\text{NO}_3^-$ , this feature appears smaller than the theory predicts, although its transition energy (380.0 eV) is in good agreement with the theoretical results. In the case of TNT, the high-energy feature arising from the nonbonding orbitals should appear at 399.4 eV, but we find that it also appears weaker. We propose that these transitions are broadened by nonradiative transitions to a degree that is greater than the constant broadening that was included in the calculations.

As in the case of  $\text{NH}_4\text{NO}_3$ , the main differences between the real-space and molecular orbital results are the shifts in the transition energies and the enhanced structure for the real-space approach. For TNT, the  $\sigma_{\text{NO}}$  bonds appear in the real-space approach higher in energy by about 1.9 eV. In addition, the high-energy feature appearing at  $\sim 397.5$  eV has, with respect to the molecular orbital results, a larger intensity and is red-shifted by 1.6 eV.

The main differences between the spectrum of TNT and those for the ionic nitrates and nitrites are observed in the 383 to 392 eV region. These differences are induced by the presence of the aromatic C atom. The StoBe-deMon simulations predict emissions, at 385.5, 388.4, and 391.9 eV, from  $\sigma_{\text{NC}}$  orbitals coupling the  $\text{NO}_2$  group to the benzene ring to different degrees. These transitions

appear smaller than the experimental features at 389.6 and 391.2 eV and we again propose that this is due to additional broadening.

**C. RDX.** The experimental RDX spectrum together with the results of the calculations is shown in Figure 8. As expected given the similarity in their structures, TNT and RDX show similar spectra. For instance, the presence of three  $\text{NO}_2$  groups results in transitions at 380.2, 393.5 to 393.7, and 394.6 eV in RDX that are equivalent to those observed in TNT at 380.0, 393.7, and 394.2 eV. The main differences between these compounds arise from the presence of the azine nitrogen atoms. These atoms induce direct and indirect effects: First, they contribute a new signal that increases the intensity of the main spectral feature in the 393 to 394 eV region. Second, they substitute a N–C bond for a N–N one, thus changing the electronic structure in the intermediate region and shifting the features between 389.6 and 391.2 eV in TNT to 397.8 eV in RDX. Finally, they alter slightly the orbital energies associated with the  $\text{NO}_2$  groups.

The StoBe-deMon simulations allow a detailed examination of these changes. They predict transitions at 379.1, 385.8, and 391.8 to 392.2 eV, associated with the nitro groups, and at 381.4, 385.0, 392.7, and 394.1 eV, arising from emission from the azine atoms. As in the experimental results, the  $\text{NO}_2$  transitions are equivalent to those observed in TNT, where they occur at 380.0, 385.5, and 392 to 394 eV. The molecular orbitals involved are also quite similar, with  $\sigma_{\text{NO}}$  (at 379.1 eV),  $\sigma_{\text{NN}}$  (at 385.8 eV), and in-plane and out-of-plane  $\pi_{\text{NN}}$  and  $\pi_{\text{NO}}$  orbitals (at 391.8 to 392.2 eV). As in all previously discussed systems, the intensity of the feature associated with the  $\sigma_{\text{NO}}$  bonds is overestimated by the theoretical results. The  $\sigma_{\text{NN}}$  orbitals are also involved in transitions localized in the azine groups, where they are responsible for the emission at 381.4 eV. This reflects the 4.4 eV difference between the N1s states in the nitro and azine groups. The azine transition at 385.0 eV is associated with emissions from the  $\sigma_{\text{NC}}$  orbitals, and is in good agreement with similar transitions in TNT (e.g., those at 385.5 eV). The remaining features have no equivalent in

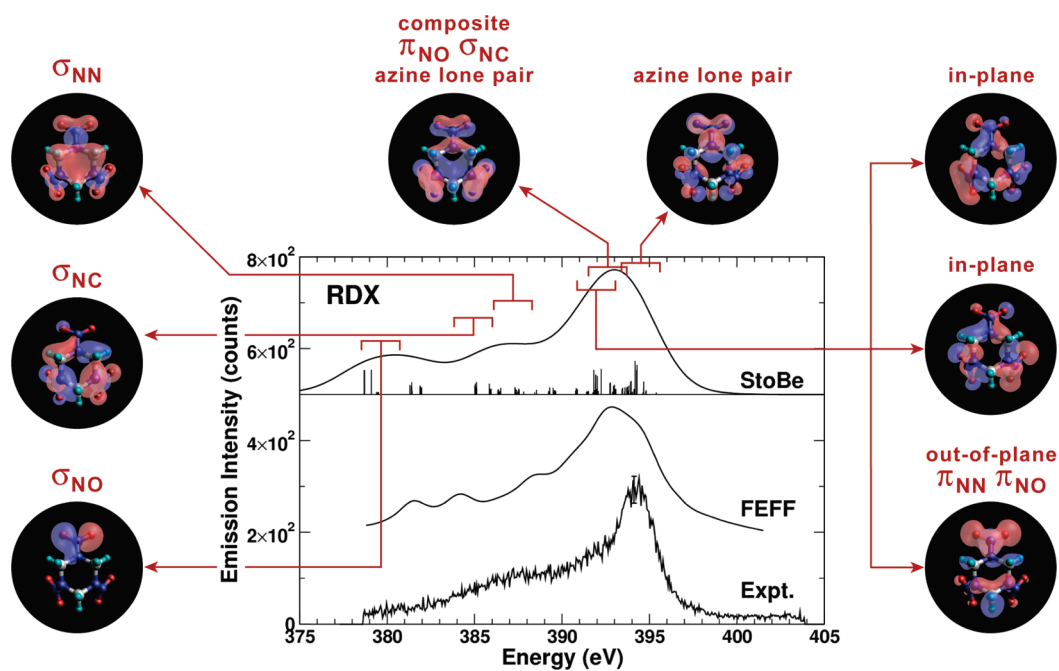


**Figure 8.** Composite spectra calculated by StoBe and FEFF compared to experimental results for RDX. The contribution of orbitals in the StoBe calculation to features in the emission spectrum is indicated.

TNT: Those predicted at 392.7 eV result from orbitals of a mixed nature, involving coupling between the in-plane  $\pi_{\text{NO}}$ ,  $\sigma_{\text{NC}}$ , and azine lone-pair nonbonding orbitals. The ones appearing at 394.1 eV result essentially from the azine lone-pair nonbonding orbitals.

Finally, RDX shows the same trends as the previous systems, with the real-space and molecular orbital approaches providing qualitatively comparable results. In addition to the more visible structure in the real-space results (clearly noticeable in the center region around 387 eV, the low-energy features are blueshifted by  $\sim 1$  eV. As in the previous case, these features are associated with  $\sigma$  bonds, in particular, the  $\sigma_{\text{NC}}$  and  $\sigma_{\text{NO}}$  bonds.

#### IV. DISCUSSION

**A. Broadening.** A uniform broadening applied to the theoretical calculations is a simple way to achieve better agreement with experiment without undue distortion of the results. The emission spectrometer resolution is not adequate to resolve individual molecular lines and the lifetime broadening of the nitrogen K level introduces further broadening of the emission lines. Given the fact that the radiative transitions of nitrogen are less than about 0.5% of the total transition rate,<sup>35</sup> short lifetime Auger transitions are expected to dominate the broadening of the X-ray emission lines.<sup>36</sup>

For the StoBe-deMon calculations, all lines were broadened using a uniform Gaussian broadening with the following full widths:  $\text{NH}_4\text{NO}_3$  2.0 eV, TNT 4.0 eV, and RDX 4.0 eV. The FEFF calculations include the broadening by adding a constant imaginary part to the self-energy (which is equivalent to Lorentzian broadening). The full widths that were used were as follows, where the first number is the extra broadening added to match experiment and the second number is the core-hole broadening that FEFF adds automatically:  $\text{NH}_4\text{NO}_3$  0.8 + 0.1 eV, TNT 2.0 + 0.1 eV, and RDX 2.0 + 0.1 eV. Inclusion of this broadening independently of energy in each spectrum allows easier visual

comparison of the calculations with the measured spectra but does not induce undue distortion of the calculated results and does not modify the measured spectra.

**B. Low- and High-Energy Features.** The features at the low- and high-energy ends of the measured spectra for all three compounds are noticeably less intense than expected from the theoretical calculations. These features are present in the spectrum but are broadened more than the uniform amount discussed above. A possible additional contribution to the broadening is relative motion from molecular vibrations because they will affect different transitions to different degrees. Neither disorder nor vibrational motion was included in the calculations. We are investigating the vibrational spectrum of these compounds and will attempt to study the vibrational motion in future work, both via improved calculations and via low-temperature measurements.

**C. Comparison Criteria.** Comparisons between the theoretical calculations and the experiment were made using the following criteria: a) The positions of the theoretical peaks should be within 1–2 eV of those observed in experiment, and b) the theoretical intensities should show the same trend as that observed in the experiment. These criteria are qualitative, but, given the broad experimental peaks, allow for reasonable assignment of each of the peaks thus providing important chemical information. The experimental energy scales for both the absorption and emission spectra (with the exception of the ammonium nitrate emission) were very carefully calibrated as discussed in part A of section II above. Careful attention was also paid to aligning the calculated spectra on a reliable energy scale. This makes the quantitative comparisons presented in this work meaningful.

#### V. CONCLUSIONS

We have investigated the X-ray emission from three energetic nitrogen compounds with considerable variation in the chemical bonding, including oxidized and reduced states. The theoretical

calculations give a good qualitative description of the data. More importantly, they show us which components of the electronic structure contribute to which parts of the emission spectrum. The StoBe-deMon molecular orbital calculations show which orbital components contribute to the features in the emission, giving a good view from a molecular chemistry viewpoint. The FEFF real-space Green's function result shows how the spectrum is filled out by calculating the electronic states in the crystal rather than discrete orbitals. It gives a density of states that begins to show spectral features of the X-ray transition in a semiquantitative way. The next refinement in the calculations would be the computationally very costly use of anisotropic potentials and the inclusion of atomic motion and disorder. Our current results go a long way toward explaining the measurements as long as the excitation is well above the N absorption edge.

In comparing the real-space Green's function and molecular orbital calculations, each method gives reasonably good agreement with the measured spectra but neither fully reproduces all aspects of the measurement. Each method has advantages both in what spectral features it calculates well and in what insight it gives into the source of those features in the emission. Which method is preferred will depend on the application and this work gives information to guide that choice. For instance, if fast, semiquantitative calculations are adequate, the real-space FEFF approach is preferable. However, the molecular orbital approach provides slightly better relative transition energies.

One of our goals is progress toward the extraction of quantitative information from X-ray emission spectra on materials whose structure is unknown. Some progress demonstrated here is that the transitions in TNT and RDX are difficult to separate a priori, but the use of theoretical calculations allows us to pinpoint the origin of the transitions. This is a quantitative advance in the use of theoretical methods for interpretation of emission spectra. Calculations are now reaching the point where, when used together, many details of the emission spectrum can be reproduced and some details of the bonding structure determined.

## ■ ASSOCIATED CONTENT

**S Supporting Information.** Input files for StoBe-deMon and FEFF used to make the calculations presented here. This material is available free of charge via the Internet at <http://pubs.acs.org>.

## ■ ACKNOWLEDGMENT

This work was supported in part by the Office of Naval Research under grant N00014-05-1-0843 (W.T.E. and F.D.V.) and in part by the U.S. Department of Energy, Office of Basic Energy Sciences grant DE-FG02-97ER45623 (J.J.R.). The Advanced Light Source is supported by the Director, Office of Science, Office of Basic Energy Sciences, of the U.S. Department of Energy under Contract No. DE-AC02-05CH11231.

## ■ REFERENCES

- (1) de Groot, F. *Chem. Rev.* **2001**, *101*, 1779.
- (2) Guo, J. *Int. J. Nanotechnol.* **2004**, *1*, 193.
- (3) Ankudinov, A. L.; Elam, W. T.; Sieber, J. R.; Rehr, J. J. *X-Ray Spectrom.* **2006**, *35*, 312.
- (4) Kim, P.-S. G.; Naftel, S. J.; Sham, T. K.; Coulthard, I.; Hu, Y.-F.; Moewes, A.; Freeland, J. W. *J. Electron Spectrosc. Relat. Phenom.* **2005**, *144–147*, 901.

- (5) Nordgren, E. *J. Phys. Scr.* **1996**, *T61*, 32.
- (6) Zimina, A.; Batchelor, D. R.; Eisebitt, S.; Schmeisser, D.; Shulakov, A.; Eberhardt, W. *Surf. Interface Anal.* **2008**, *40*, 958.
- (7) Terauchi, M.; Koike, M.; Fukushima, K.; Kimura, A. *J. Electron Microsc. (Tokyo)* **2010**, *59*, 251.
- (8) Wollman, D. A.; Nam, S. W.; Newbury, D. E.; Hilton, G. C.; Irwin, K. D.; Bergren, N. F.; Deiker, S.; Rudman, D. A.; Martinis, J. M. *Nucl. Instrum. Methods Phys. Res., Sect. A* **2000**, *444*, 145.
- (9) MacNaughton, J. B.; Moewes, A.; Kurmaev, E. Z. *J. Phys. Chem. B* **2005**, *109*, 7749.
- (10) MacNaughton, J. B.; Wilks, R. G.; Lee, J. S.; Moewes, A. *J. Phys. Chem. B* **2006**, *110*, 18180.
- (11) Harada, Y.; Takeuchi, T.; Kino, H.; Fukushima, A.; Takakura, K.; Hieda, K.; Nakao, A.; Shin, S.; Fukuyama, H. *J. Phys. Chem. A* **2006**, *110*, 13227.
- (12) Jupp, I. D.; Durrant, P. T.; Ramsden, D.; Carter, T.; Dermody, G.; Pleasants, I. B.; Burrows, D. *IEEE Trans. Nucl. Sci.* **2000**, *47*, 1987.
- (13) Jia, J. J.; Callcott, T. A.; Yurkas, J.; Ellis, A. W.; Himpel, F. J.; Samant, M. G.; Stohr, J.; Ederer, D. L.; Carlisle, J. A.; Hudson, E. A.; Terminello, L. J.; Shuh, D. K.; Perera, R. C. *Rev. Sci. Instrum.* **1995**, *66*, 1394.
- (14) Hitchcock, A. P.; Brion, C. E. *J. Electron Spectrosc. Relat. Phenom.* **1980**, *18*, 1.
- (15) Kakar, S.; Nelson, A. J.; Treusch, R.; Heske, C.; van Buuren, T.; Jimenez, I.; Pagoria, P.; Terminello, L. J. *Phys. Rev. B* **2000**, *62*, 15666.
- (16) Vinogradov, A. S.; Preobrajenski, A. B.; Molodtsov, S. L.; Krasnikov, S. A.; Szargan, R.; Knop-Gericke, A.; Hävecker, M. *Chem. Phys.* **1999**, *249*, 249.
- (17) Aduru, S.; Contarini, S.; Rabalais, J. W. *J. Phys. Chem.* **1986**, *90*, 1683.
- (18) Preobrajenski, A. B.; Vinogradov, A. S.; Molodtsov, S. L.; Krasnikov, S. K.; Chassé, T.; Szargan, R.; Laubschat, C. *Phys. Rev. B* **2002**, *65*, 205116.
- (19) Triguero, L.; Pettersson, L.; Agren, H. *J. Phys. Chem. A* **1998**, *102*, 10599.
- (20) Ankudinov, A. L.; Ravel, B.; Rehr, J. J.; Conradson, S. D. *Phys. Rev. B* **1998**, *58*, 7565.
- (21) Ankudinov, A. L.; Bouldin, C. E.; Rehr, J. J.; Sims, J.; Hung, H. *Phys. Rev. B* **2002**, *65*, 104107.
- (22) Choi, C. S.; Mapes, J. E.; Prince, E. *Acta Crystallogr.* **1972**, *B28*, 1357.
- (23) Choi, C. S.; Prince, E. *Acta Crystallogr.* **1972**, *B28*, 2857.
- (24) Carper, W. R.; Davis, L. P.; Extine, M. W. *J. Phys. Chem.* **1982**, *86*, 459.
- (25) Kutzelnigg, W.; Fleischer, U.; Schindler, M. *NMR Basic Principles Progress* **1990**, *23*, 167.
- (26) Godbout, N.; Salahub, D. R.; Andzelm, J.; Wimmer, E. *Can. J. Chem.* **1992**, *70*, 560.
- (27) Becke, A. D. *Phys. Rev. A* **1988**, *38*, 3098.
- (28) Perdew, J. P.; Wang, Y. *Phys. Rev. B* **1986**, *33*, 8800.
- (29) Hedin, L.; Lundqvist, S. *Solid State Phys.* **1969**, *23*, 1.
- (30) Kresse, G.; Furthmüller, J. *Phys. Rev. B* **1996**, *54*, 11169.
- (31) Perdew, J. P.; Burke, K.; Ernzerhof, M. *Phys. Rev. Lett.* **1996**, *77*, 3865.
- (32) Henkelman, G.; Arnaldsson, A.; Jónsson, H. *Comput. Mater. Sci.* **2006**, *36*, 354.
- (33) Preobrajenski, A. B.; Vinogradov, A. S.; Krasnikov, S. A.; Szargan, R.; Mårtensson, N. *Phys. Rev. B* **2004**, *69*, 115116.
- (34) Kosuch, N.; Tegeler, E.; Wiech, G.; Faessler, A. *J. Electron Spectrosc. Relat. Phenom.* **1978**, *13*, 263.
- (35) Hubbell, J. H.; Trehan, P. N.; Singh, N.; Chand, B.; Mehta, D.; Garg, M. L.; Garg, R. R.; Singh, S.; Puri, S. *J. Phys. Chem. Ref. Data* **1994**, *23*, 339.
- (36) Heitler, W. *The Quantum Theory of Radiation*, 3rd ed.; Oxford University Press: Oxford, 1966; pp 185–189.